JOURNAL OF THEORETICAL
AND APPLIED MECHANICS
https://doi.org/10.15632/jtam-pl/200944
ONLINE FIRST

STUDY ON NOISE CONTROL OF TUNABLE FLUID-SOLID COUPLED PHONONIC CRYSTAL STRUCTURES IN THE CONTEXT OF ENCLOSED FISH FARMS

Denghui QIAN*, Jiawei ZHUANG, Shengke ZHANG

School of Naval Architecture & Ocean Engineering, Jiangsu University of Science and Technology, Zhenjiang 212100, Jiangsu, China

*corresponding author, *dhqian@just.edu.cn*

Identifying innovative strategies to mitigate underwater noise, which exerts a wide array of detrimental effects on fish physiology, behavior, biodiversity, and entire aquatic ecosystems, presents a significant scientific challenge in the conservation of marine environments. The sources of underwater noise are well-documented and encompass marine transportation, geological exploration, and various industrial activities in marine environments. In addressing these concerns, we propose a solid cylindrical structure of fluid-solid coupled phononic crystals that leverages the local resonance mechanism. The finite element method is employed to analyze the bandgap characteristics and acoustic transmission loss of the finite periodic structure. Furthermore, we investigate the influence of structural parameters on the attenuation frequency range of the bandgap. Building on this analysis, we design a hollow cylindrical structure of fluid-solid coupled phononic crystals, which demonstrates superior sound insulation performance for frequencies below 300 Hz. Additionally, we propose filling the hollow cylinders with fluid to modulate the bandgap of the structure. This study introduces an innovative approach to controlling underwater noise and modulating the phononic crystal bandgap, providing essential insights into the preservation of aquatic ecosystems and mitigating the detrimental influence of underwater noise on marine organisms.

Keywords: phononic crystals; fluid-solid coupling; underwater noise; enclosed fish farm; transmission curve.

1. Introduction

In recent years, intensified human exploration of the oceans has escalated anthropogenic activities in the marine environment, leading to increased underwater noise that adversely affects the health and behavior of numerous fish and marine mammals. High-frequency noise can induce short-term changes in physiological parameters such as oxygen consumption, cortisol, glucose, and lactic acid levels in fish (Herbert-Read *et al.*, 2017), thereby altering their swimming speed, depth, and direction, ultimately impacting fish shoals. Low-frequency noise compromises the auditory sensitivity of fish (Zhan *et al.*, 2023), resulting in temporary or permanent shifts in their auditory thresholds. Prolonged exposure to high-intensity low-frequency noise can impair species identification, reproductive behaviors, and population communication in fish. Li *et al.* (2022) monitored underwater environmental noise at a depth of 35 meters and concluded that wind on the sea surface is the primary factor influencing frequencies above 500 Hz, whereas, for frequencies below 500 Hz, human navigation activities are the predominant factor. Consequently, an increasing number of researchers are concentrating on anthropogenic low-frequency noise, as its impact on fish has emerged as a serious ecological concern.

Ocean noise primarily comprises natural background noise from wind, waves, tides, rainfall, and earthquakes; biological noise from fish movements, feeding, and mating; and anthropogenic noise (Lu *et al.*, 2024; Huang *et al.*, 2023). Anthropogenic noise encompasses marine shipping (Helal *et al.*, 2024), geological exploration, sonar (Fan *et al.*, 2017), as well as industrial and

construction activities in marine environments. Owing to the properties of sound in water – such as rapid propagation speed, low transmission loss, and extended transmission distance – industrial activities like piling (Jia *et al.*, 2024), dredging, offshore wind turbine operation (Zhang *et al.*, 2017), and underwater blasting can generate noise that affects areas ranging from 100 meters to over 1000 meters from the source (Zhang *et al.*, 2012).

Numerous studies have investigated the effects of low-frequency noise on fish physiology, behavior, and population dynamics. Shi *et al.* (2010) examined the impact of ship noise on cortisol levels in large yellow croaker, finding a significant increase in blood cortisol levels under ship noise exposure. Ye *et al.* (2023) studied the effects of low-frequency vibration stimuli on the behavior and physiology of large yellow croaker and discovered that the fish exhibited heightened sensitivity to 200 Hz vibration stimuli. Lin *et al.* (2020) investigated the impact of ship noise sound pressure levels on the behavior of juvenile large yellow croakers, revealing that increasing sound pressure levels intensified stress avoidance behaviors. Crovo *et al.* (2015) discovered that the auditory thresholds of blacktail shiner significantly increased across various noise frequencies when exposed to traffic road noise.

As human activities in the ocean continue to escalate, noise from diverse sources has become increasingly prevalent. Implementing effective control measures for underwater noise is imperative to prevent irreversible damage to fish diversity and underwater ecosystems. Noise arises from the propagation effects of elastic waves within structures and the coupling interactions between these waves and media such as air and water. In recent decades, the concept of phononic crystals has invigorated the study of elastic wave propagation characteristics in the field of physics (Wu *et al.*, 2016a; 2016b; Yin *et al.*, 2022). The bandgap properties of phononic crystals effectively suppress the propagation of elastic waves within the bandgap range, offering novel approaches for underwater noise reduction.

Li *et al.* (2024) focused on the wooden frame structure of high-speed train floors and designed a hybrid structure combining wooden frames with phononic crystals, leveraging the phononic crystal theory. They conducted a systematic analysis of the bandgap characteristics and sound insulation performance of the phononic crystal structure. Liu *et al.* (2023) designed the Helmholtz-type phononic crystal featuring an adjustable cavity structure. Yao *et al.* (2021) proposed the smooth finite element calculation method for two-dimensional fluid/solid phononic crystals and validated it through multiple two-dimensional phononic crystal examples. Jiang *et al.* (2009) developed an underwater sound-absorbing material composed of locally resonant phononic woodpile. Theoretical and experimental results demonstrated that the locally resonant phononic woodpile exhibited excellent sound absorption properties due to the synergy of locally resonant unit structures and multi-scale woodpile structures. Wang *et al.* (2022) tackled the challenge of low-frequency sound absorption in acoustic coatings by developing a composite structure that integrates locally resonant structures within the cavity coating.

In summary, this paper addresses the challenge of underwater anthropogenic noise adversely affecting fish diversity and underwater ecosystems by designing a solid cylindrical structure of fluid-solid coupled phononic crystals leveraging the local resonance mechanism. The bandgap characteristics and acoustic transmission loss of the finite periodic structure were analyzed using the finite element method, and the impact of structural parameters on the bandgap attenuation frequency range was investigated. Building on this analysis, a hollow cylindrical structure of fluid-solid coupled phononic crystals was designed. It is proposed to fill the hollow cylinders with fluid to modulate the bandgap of the structure, offering a novel approach for underwater noise control and phononic crystal bandgap regulation.

2. Model and calculation method

Based on the mechanism of local resonance phononic crystal bandgap formation, this paper establishes a fluid-solid coupled phononic crystal solid cylinder unit cell model, utilizing water

as the base material, as illustrated in Fig. 1a. Building on this foundation, a novel fluid-solid coupled phononic crystal hollow cylinder unit cell model is designed by perforating the scatterer, as depicted in Fig. 1b. Fixed constraint conditions are applied at the bottom of the cylinder to better match the structure's application environment. The geometric and material parameters of the structural model are detailed in Tables 1 and 2. Figure 2 presents a schematic diagram of the arrangement of the fluid-solid coupled phononic crystal structure in an enclosure fishery. The fluid-solid coupled phononic crystal structures are periodically arranged on a steel plate, with their bases secured to the plate. The steel plate can be attached to the four pile centers of the enclosure fishery using clamps.

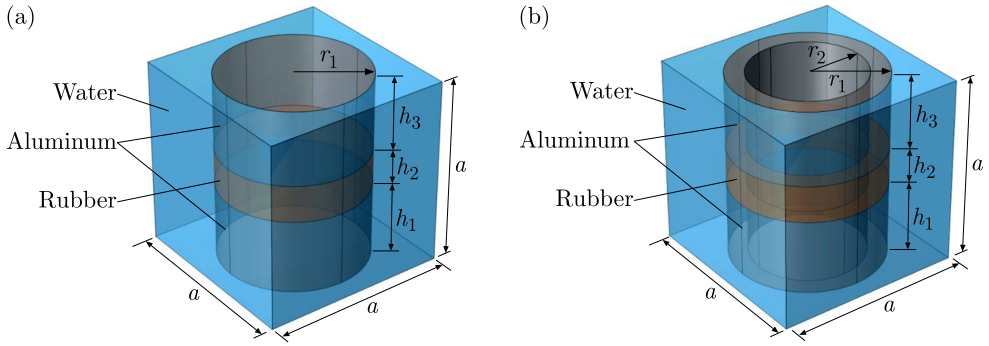

Fig. 1. Single-cell model of fluid-solid coupled phononic crystals: (a) solid cylinder; (b) hollow cylinder.

Table 1. Material parameters.

Material	Density [kg/m^3]	Young's modulus [GPa]	Poisson's ratio	Velocity [m/s]
Aluminum	2700	70	0.33	–
Rubber	1100	1.49e-3	0.49	–
Water	1000	–	–	1490

Table 2. Structural parameters.

Parameter [m]	a	h_1	h_2	h_3	r_1	r_2
Value	1	0.4	0.2	0.4	0.4	0.3

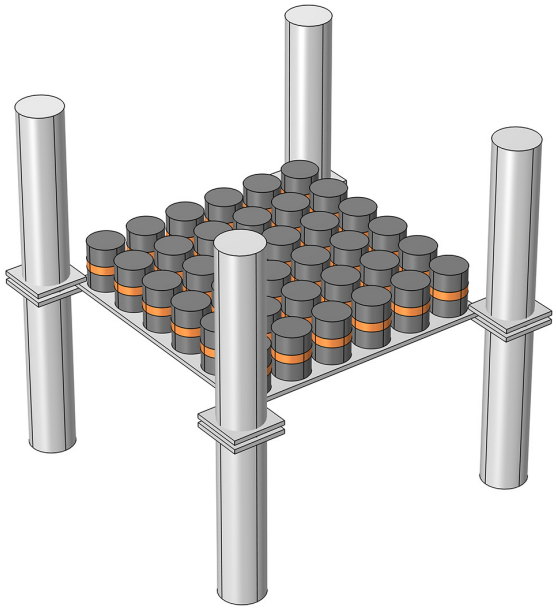

Fig. 2. Schematic arrangement of fluid-solid coupled phononic crystal structure.

Drawing on the propagation characteristics of elastic waves in phononic crystals and the periodicity theory, this paper employs the finite element method for calculations by applying Floquet periodic boundary conditions on the unit cell boundaries and introducing the Bloch wave vector **k** for solutions. These computations are performed using COMSOL Multiphysics. The discrete form of the phononic crystal unit cell characteristic equation is given as

$$(\mathbf{K} - \omega^2 \mathbf{M}) \cdot \mathbf{u} = 0, \tag{2.1}$$

where **K** represents the stiffness matrix, **M** denotes the mass matrix, **u** signifies the displacement matrix of the unit cell. Mechanical waves propagate as vector waves (transverse and longitudinal) in solids, whereas in fluids, they propagate solely as longitudinal waves. Therefore, when calculating the band structure of fluid-solid coupled phononic crystals, it is imperative to partition the fluid and solid domains and apply appropriate boundary conditions at the fluid-solid interface. At the fluid-solid interface, the normal displacement and force must be continuous:

$$U_s \cdot \mathbf{n} = U_f \cdot \mathbf{n}, \qquad p \cdot \mathbf{n} = \sigma \cdot \mathbf{n}, \tag{2.2}$$

where U_s and U_f represent the displacements in the solid and fluid, respectively, **n** denotes the normal vector at the fluid-solid interface, p signifies the fluid pressure at the interface, σ is the stress tensor of the solid at the interface:

$$U_s(r + a) = e^{i(k \cdot a)} U_s(r), \qquad p(r + a) = e^{i(k \cdot a)} p(r). \tag{2.3}$$

In a two-dimensional phononic crystal, $\mathbf{r}(x, y)$ denotes the position vector, and $\mathbf{k}(x, y)$ represents the wave vector. By integrating the characteristic equation with boundary conditions, the eigenfrequencies can be determined for a given wave vector **k**. In COMSOL, scanning the wave vector **k** along the boundary of the irreducible Brillouin zone yields the band structure diagram of the phononic crystal.

3. Numerical results and analysis

3.1. Band structure and transmission curve of the fluid-solid coupled phononic crystal solid cylinder structure

Figure 3a illustrates the band structure of the fluid-solid coupled phononic crystal solid cylinder structure, with the material and geometric parameters of the unit cell detailed in Tables 1 and 2, respectively. To validate the accuracy of the band structure diagram, Fig. 3b presents the acoustic transmission loss curve for the finite periodic structure. The unit cells are arranged

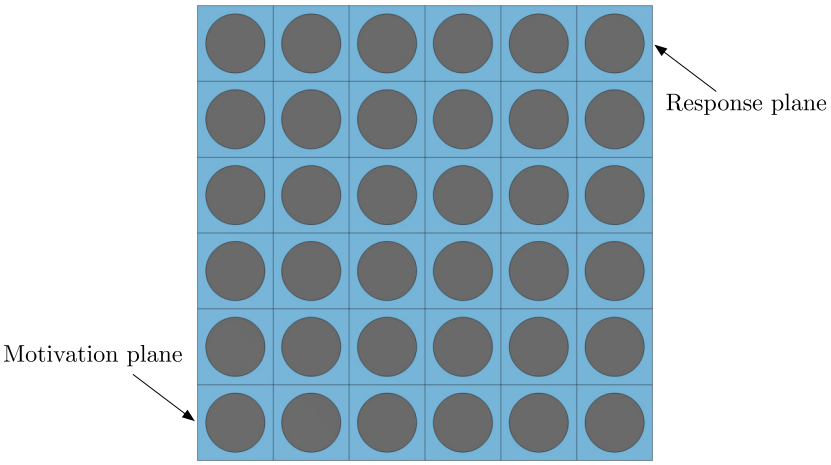

Fig. 3. Finite element calculation model.

in a square lattice periodic configuration horizontally to form a two-dimensional fluid-solid coupled phononic crystal structure with six periods, as depicted in Fig. 3. The background pressure field serves as the incident acoustic excitation, with a sound pressure amplitude of 1 Pa. The sound wave is incident perpendicularly onto the phononic crystal structure as a plane wave, and the response is measured at the diagonal of the incident end.

Figure 4a reveals that the first complete bandgap range of the fluid-solid coupled phononic crystal solid cylinder structure spans from 17.8 Hz to 46 Hz, while the second bandgap range extends from 126 Hz to 153.1 Hz. It is noteworthy that numerous flat bands exist within the second bandgap; these are local resonance bands and do not impact the structural bandgap. Figure 4b indicates that elastic waves propagate in the finite periodic structure with significant sound insulation effects in the ranges of 17.8 Hz–46 Hz and 126 Hz–153.1 Hz, particularly in the range of 17.8 Hz–46 Hz, where the sound insulation level can reach up to 168 dB. The sound attenuation frequency range aligns with the bandgap frequency range of the infinite periodic structure depicted in Fig. 4a. To further elucidate the bandgap formation mechanism, characteristic modes at the beginning and end frequencies of the bandgap are analyzed, as shown in Fig. 5.

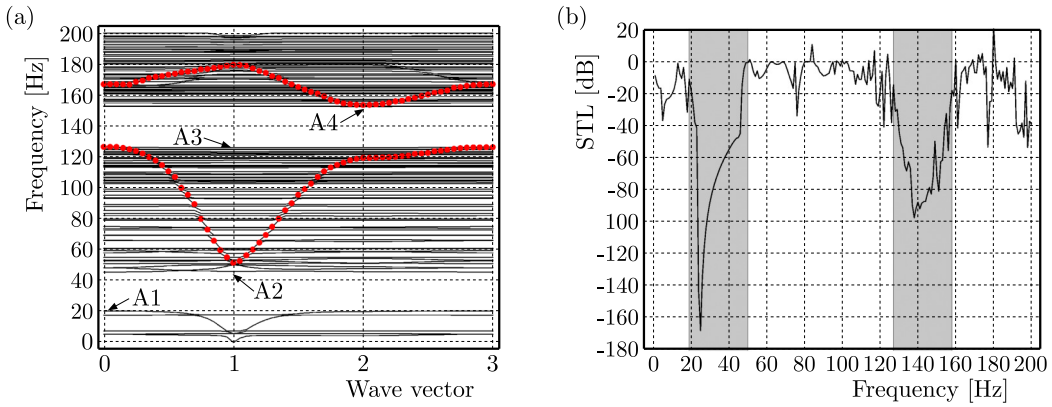

Fig. 4. Band structure (a) and sound transmission loss (b) of solid cylinder structure of fluid-solid coupled phononic crystals.

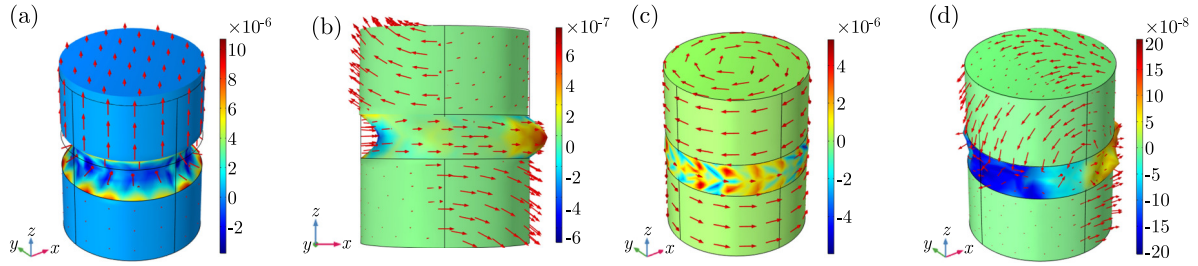

Fig. 5. Vibration modal diagrams: (a) A1; (b) A2; (c) A3; (d) A4.

The vibration modes depicted in Fig. 5 indicate that in mode A1, the rubber and the upper aluminum column in the scatterer vibrate longitudinally along the z-axis, while the lower aluminum column remains stationary. Modes A2 and A4 belong to the same vibration mode, exhibiting torsional vibration of the hard scatterer aluminum in the x-, z-plane attributed to the fixed constraint at the bottom of the column. In mode A3, the hard scatterer exhibits torsional vibration in the x-, z-plane without movement in the z-direction. The upper and lower aluminum columns undergo torsional vibrations in opposite directions, achieving dynamic equilibrium. When elastic waves propagate through this structure, these vibration modes couple to form two vibration bandgaps, 17.8 Hz–46 Hz and 126 Hz–153.1 Hz.

To further illustrate the attenuation characteristics of this structure, Fig. 6a presents the sound pressure distribution for the finite periodic fluid-solid coupled phononic crystal solid cylinder structure at a frequency within the bandgap attenuation range. A sound pressure of 1 Pa is applied in the x-direction on the excitation surface, with a plane wave incident perpendicularly to the structure at a frequency of $f = 46$ Hz. Figure 6a demonstrates that when excitation is applied to one side of the structure, the sound wave cannot propagate through it, resulting in significant attenuation of the sound pressure on the response surface located on the opposite side compared to the excitation surface. In contrast, Fig. 6b illustrates the sound pressure distribution for the structure at a frequency outside the bandgap attenuation range, with a selected frequency of $f = 51$ Hz. It is evident that when excitation is applied to one side of the structure, the sound wave propagates effectively through the structure without any attenuation.

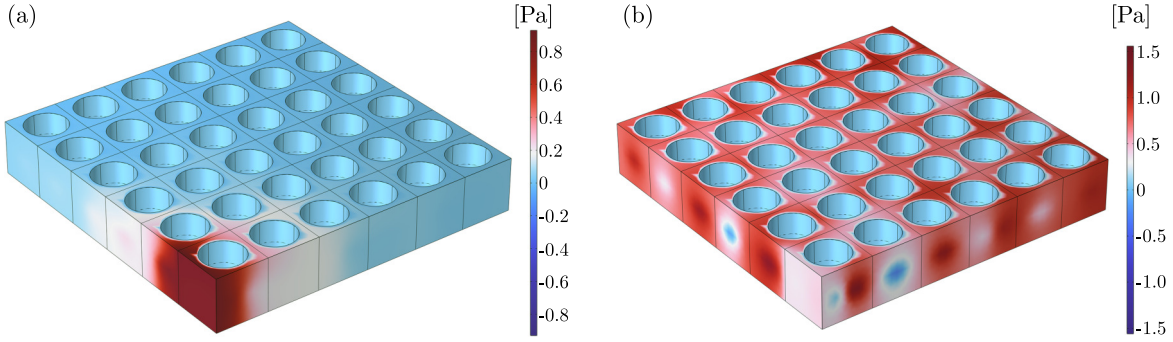

Fig. 6. Sound pressure diagrams of solid cylinder structures of finite-period fluid-solid coupled phononic crystals with frequencies falling in (a) the bandgap ($f = 46$ Hz) and (b) the non-bandgap ($f = 51$ Hz) attenuation band.

3.2. Influence of structural parameters on the bandgap attenuation range of the solid cylinder structure

The parameters used for the calculations align with those presented in Fig. 1a and are detailed in Tables 1 and 2. The lattice constant a, the radius of the solid cylinder r_1, and the thickness of the intermediate rubber layer h are chosen as influencing parameters. Since the total height of the column must remain constant according to the control variable method, the analysis of the thickness h of the intermediate rubber layer is adjusted to the proportion of the rubber layer within the column. These parameters are utilized to investigate the influence of structural geometric parameters on the starting frequency, cutoff frequency, and bandwidth of the bandgap attenuation range. For clarity in this section, SF denotes the starting frequency, CF denotes the cutoff frequency, and W denotes the bandgap width. More specifically, SF-1 and SF-2 denote the starting frequencies of the first and the second bandgaps, respectively; CF-1 and CF-2 denote the cutoff frequencies of the first and second bandgaps, respectively; and W-1 and W-2 denote the widths of the first and second bandgaps, respectively.

For the fluid-solid coupled phononic crystal solid cylinder structure, as illustrated in Figs. 7a and 7b, increasing the lattice constant keeps the starting frequency of the first bandgap attenuation range nearly constant, while slightly decreasing the starting frequency of the second bandgap attenuation range. The cutoff frequencies of both the first and second bandgap attenuation ranges exhibit an upward trend. Consequently, as the lattice constant increases, the widths of both bandgaps expand. Increasing the radius of the solid cylinder reveals that the starting frequency of the first bandgap attenuation range slightly increases, whereas the starting frequency of the second bandgap attenuation range slightly decreases. The cutoff frequencies of both the first and second bandgap attenuation ranges decrease. Therefore, the widths of both bandgaps demonstrate a decreasing trend, as shown in Figs. 7c and 7d. Figures 7e and 7f illustrate that

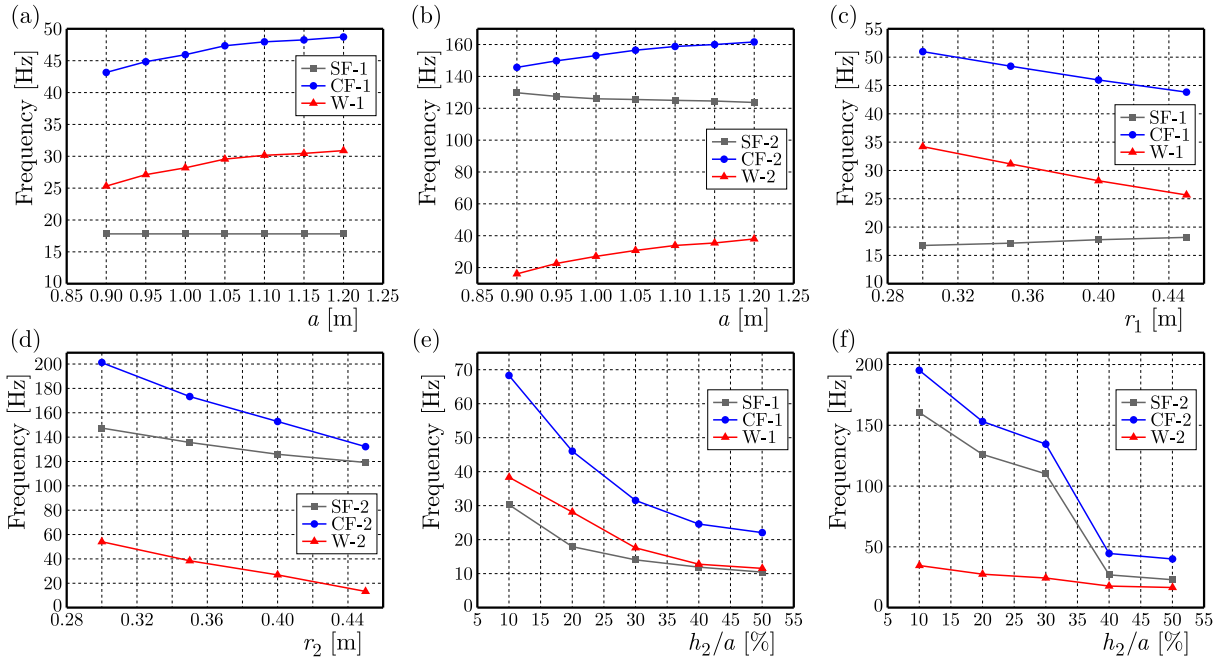

Fig. 7. Influence law of structural parameters on the bandgap attenuation band of solid cylinder structures.

the proportion of the rubber layer significantly impacts the bandgap attenuation range. As the proportion of the rubber layer in the solid cylinder gradually increases, the starting and cut-off frequencies of both the first and second bandgap attenuation ranges decrease significantly, along with the widths of both bandgaps. It is important to note that when the proportion of the rubber layer exceeds 30 %, the attenuation range of the second bandgap significantly decreases.

3.3. Band structure and transmission curve of the fluid-solid coupled phononic crystal hollow cylinder structure

Figure 8a illustrates the band structure of the fluid-solid coupled phononic crystal hollow cylinder structure, with the material and geometric parameters of the unit cell detailed in Tables 1 and 2. To validate the accuracy of the band structure diagram, Fig. 8b presents the acoustic transmission loss curve for the finite periodic structure. The unit cells are arranged in a square lattice periodic configuration horizontally to form a two-dimensional fluid-solid coupled

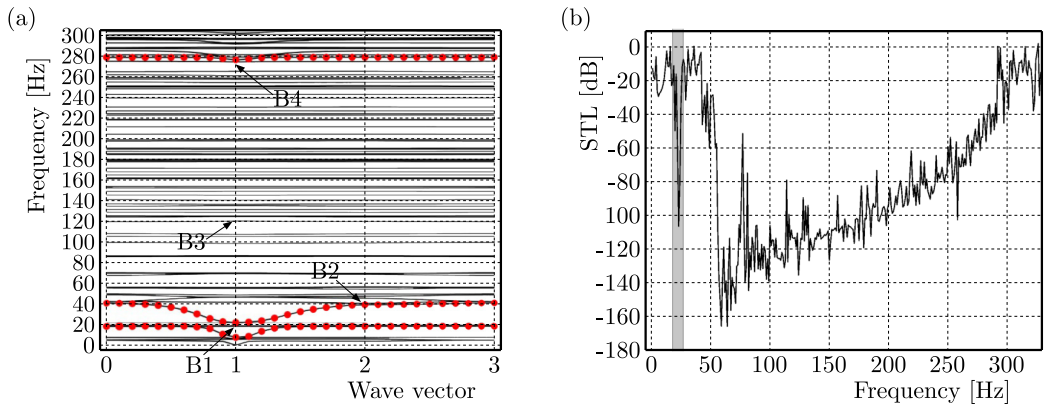

Fig. 8. Band structure (a) and sound transmission loss (b) of hollow cylinder structure of fluid-solid coupled phononic crystals.

phononic crystal structure with six periods. The background pressure field serves as the incident acoustic excitation, with a sound pressure amplitude of 1 Pa. The sound wave is incident perpendicularly onto the phononic crystal structure as a plane wave, and the response is measured at the diagonal of the incident end.

Figure 8a shows that the first complete bandgap range of the fluid-solid coupled phononic crystal hollow cylinder structure spans from 18 Hz to 21.8 Hz, while the second bandgap range extends from 46.3 Hz to 275.4 Hz. Although many flat bands exist within the second bandgap, their impact on the structural bandgap is negligible. Figure 8b indicates that when elastic waves propagate in the finite periodic structure, significant sound insulation occurs in the ranges of 18 Hz–21.8 Hz and 46.3 Hz–275.4 Hz. The sound attenuation frequency range aligns with the complete bandgap opening frequency range of the infinite periodic structure depicted in Fig. 8a. Within the bandgap range illustrated in Fig. 8, the fluid-solid coupled phononic crystal hollow cylinder structure exhibits no intrinsic modes. To further elucidate the mechanism of bandgap formation, characteristic modes at the starting and cutoff frequencies of the bandgap are analyzed, as shown in Fig. 9.

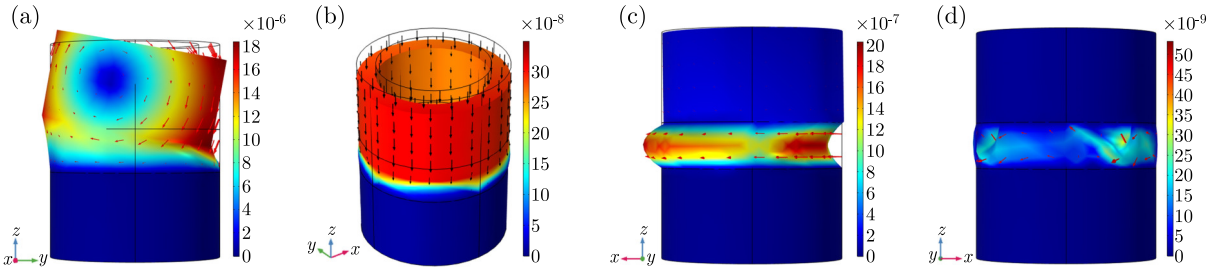

Fig. 9. Vibration modal diagrams: (a) B1; (b) B2; (c) B3; (d) B4.

The vibration modes shown in Fig. 9 reveal that in mode B1, the scatterer undergoes torsional vibration, with the lower aluminum column remaining stationary due to the fixed constraint at the bottom of the column, while the rubber and upper aluminum column undergo torsional vibration in the y-, z-plane. In mode B2, the rubber and upper aluminum column in the scatterer vibrate longitudinally along the z-axis, while the lower aluminum column remains stationary. In mode B3, the rubber and upper aluminum column in the scatterer vibrate laterally in the x-, y-plane, while the lower aluminum column remains stationary. Mode B4 involves torsional vibration of the scatterer, with the middle rubber layer undergoing torsional vibration in the x-, y-plane and very slight movement in the z-direction. B4 corresponds to a point at the cutoff frequency of the flat bandgap, as shown in Fig. 9d. The displacement field at mode B4 is much smaller compared to other modes, indicating that at point B4, the structure is nearing equilibrium, and the local resonance mode will no longer be excited, thus closing the bandgap. When elastic waves propagate in this structure, these vibration modes couple to form two vibration bandgaps, 18 Hz–21.8 Hz and 46.3 Hz–275.4 Hz. The hollow cylinder structure can form an improved low-frequency bandgap, which, compared to a solid cylinder structure of the same size, widens the low-frequency bandgap, enhances sound insulation, and better achieves low-frequency broadband noise reduction.

To further illustrate the attenuation characteristics of this structure, Fig. 10a shows the sound pressure distribution for the finite periodic fluid-solid coupled phononic crystal solid cylinder structure at a frequency within the bandgap attenuation range. A sound pressure of 1 Pa is applied in the x-direction on the excitation surface, with a plane wave incident perpendicularly to the structure at a frequency of $f = 84$ Hz. Figure 10a demonstrates that when the excitation is applied to one side of the structure, the sound wave cannot propagate through it, resulting in significant attenuation of the sound pressure on the response surface located on the opposite side compared to the excitation surface. In contrast, Fig. 10b illustrates the sound pressure distri-

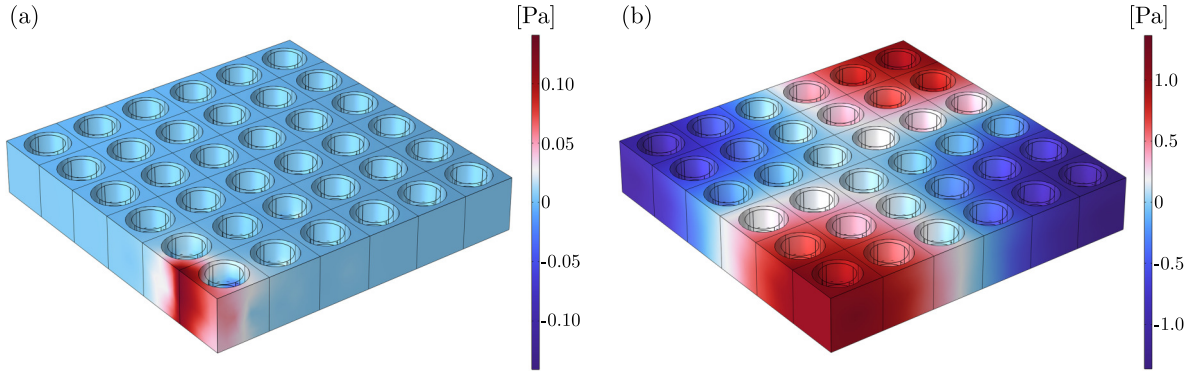

Fig. 10. Sound pressure diagrams of hollow cylinder structures of finite-period fluid-solid coupled phononic crystals with frequencies falling in (a) the bandgap ($f = 84\,\mathrm{Hz}$) and (b) the non-bandgap ($f = 16\,\mathrm{Hz}$) attenuation band.

bution for the structure at a frequency outside the bandgap attenuation range, with a selected frequency of $f = 16\,\mathrm{Hz}$. It is evident that when the excitation is applied to one side of the structure, the sound wave propagates effectively through the structure without any attenuation.

3.4. Influence of structural parameters on the bandgap attenuation range of the hollow cylinder structure

The parameters used for the calculations align with those shown in Fig. 1b and are detailed in Tables 1 and 2. Subsection 3.2 of this paper has already examined the influence of the basic structural parameters of the fluid-solid coupled phononic crystal solid cylinder on the bandgap attenuation range, so it will not be reiterated here. In the fluid-solid coupled phononic crystal hollow cylinder, the aperture r_2 is selected as the influencing parameter to investigate the impact of structural geometric parameters on the starting frequency, cutoff frequency, and bandwidth of the bandgap attenuation range.

For the fluid-solid coupled phononic crystal hollow cylinder structure, as the aperture radius increases, as shown in Fig. 11a, the starting frequency of the first bandgap attenuation range remains nearly constant, while the cutoff frequency decreases slightly, resulting in a narrower first bandgap. Figure 11b indicates that the starting frequency of the second bandgap attenuation range decreases slightly, while the cutoff frequency increases significantly, leading to a substantial widening of the second bandgap.

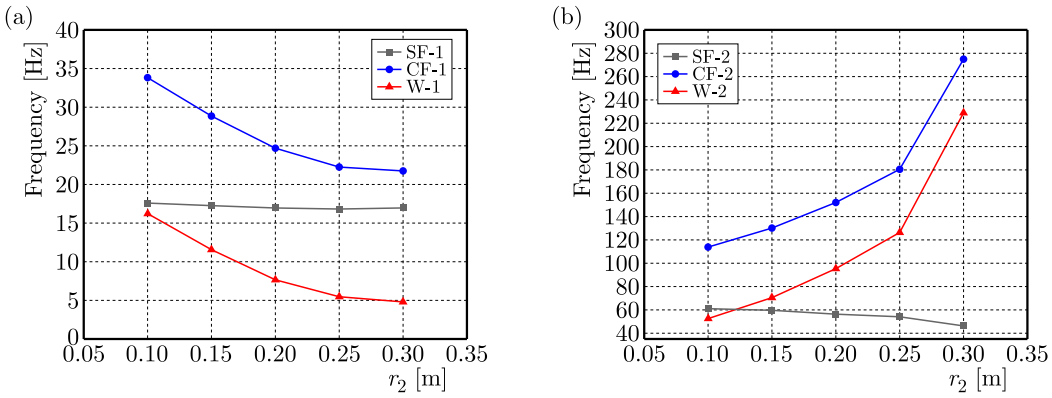

Fig. 11. Influence law of structural parameters on the bandgap attenuation band of hollow cylinder structures.

3.5. Optimization of the fluid-solid coupled phononic crystal hollow cylinder structure

The previous analysis examined the influence of structural parameters on the bandgap attenuation range of fluid-solid coupled phononic crystal solid and hollow cylinder structures, concluding that altering structural parameters allows control over the attenuation range to target specific frequency ranges. Although this method effectively controls the propagation of elastic waves, altering structural parameters is cumbersome and not economical. In contrast, filling the hollow cylinder structure of fluid-solid coupled phononic crystals with fluid can achieve tunability of the elastic wave bandgap. We investigated the impact of the fluid fill height in the hollow cylinder structure on the bandgap attenuation range. The parameters used for the calculations align with those shown in Fig. 1b and are detailed in Tables 1 and 2.

As shown in Fig. 12, filling the hollow cylinder with fluid up to 0.4 m lowered the bandgap attenuation range by 2.6 Hz, while the center frequency of the bandgap decreased by 15.3 %. When the fluid fill height in the hollow cylinder is between 0.4 m and 0.6 m, the starting frequency of the first bandgap remains essentially unchanged, while the cutoff frequency exhibits an increasing trend. When the fluid fill height in the hollow cylinder exceeds 0.6 m, the starting frequency of the first bandgap decreases by 2.2 Hz, and the cutoff frequency increases by 14.2 Hz, thereby widening the bandgap by 16.4 Hz, or 56.6 %. Therefore, through the study of fluid filling in the fluid-solid coupled phononic crystal hollow cylinder structure, we have demonstrated that fluid filling can be used to control the transmission of elastic waves within a specific frequency range, thus adjusting the position of the bandgap attenuation range.

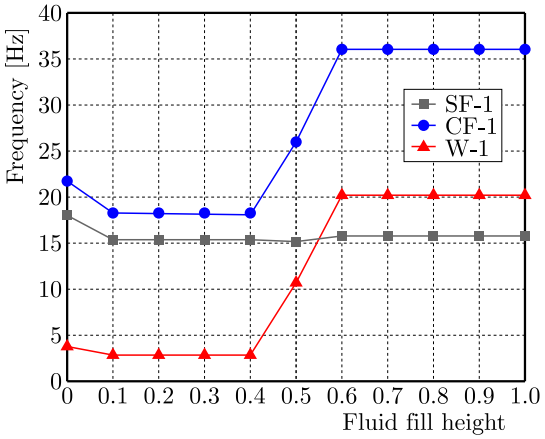

Fig. 12. First bandgap attenuation band and bandgap width versus fluid fill height.

4. Conclusion

As human activities in the ocean continue to intensify, anthropogenic underwater noise has had a profound impact on fish biodiversity and marine ecosystems. This paper addresses the influence of underwater noise on the aquaculture of marine enclosed fisheries and introduces a fluid-solid coupled phononic crystal solid cylinder structure, leveraging the local resonance mechanism inherent in phononic crystals. The band structure and acoustic transmission loss curve of the finite periodic structure were computed utilizing the finite element method, facilitating a comprehensive study of its bandgap characteristics. Building upon this, a fluid-solid coupled phononic crystal hollow cylinder structure was proposed. The bandgap characteristics of fluid-solid coupled solid and hollow cylinder structures were compared and analyzed, and the effects of various structural parameters on the bandgap attenuation range of the fluid-solid coupled phononic crystal structure were meticulously examined. Furthermore, the study proposed filling the fluid-solid coupled phononic crystal hollow cylinder structure with fluid to modulate the low-frequency bandgap. The primary conclusions are as follows:

- Analysis of the band structure and acoustic transmission loss curve revealed that the fluid-solid coupled phononic crystal solid cylinder structure, utilizing water as the matrix and solid composite materials as scatterers, can form a low-frequency bandgap and exhibits excellent sound insulation properties, thereby effectively controlling the propagation of underwater noise.
- Comparative analysis of the bandgap characteristics between the fluid-solid coupled phononic crystal solid cylinder structure and the hollow cylinder structure indicated that the hollow cylinder structure can establish a superior low-frequency bandgap. Compared to the solid cylinder structure of equivalent dimensions, the hollow cylinder structure significantly broadens the low-frequency bandgap, enhances sound insulation, achieves superior low-frequency broadband noise reduction, and is more lightweight and cost-effective.
- By infusing the fluid-solid coupled phononic crystal hollow cylinder structure with fluid, the transmission of elastic waves within a specified frequency range can be controlled, thereby adjusting the position of the bandgap attenuation range and enhancing the structure's applicability across various marine noise environments.

The fluid-solid coupled phononic crystal column structure presented in this study exhibits outstanding sound insulation capabilities for noise frequencies below 300 Hz in marine environments. This structure holds significant promise in mitigating the harmful effects of anthropogenic underwater noise on fish physiology, behavior, and populations, thereby enhancing the health of the aquatic ecosystem and safeguarding fish biodiversity.

Acknowledgments

This research was supported by the National Natural Science Foundation of China (no. 52301373), the Young Elite Scientists Sponsorship Program by CAST (2022QNRC001) and the Natural Science Foundation of Jiangsu Higher Education Institutions of China (no. 22KJB580005).

References

1. Crovo, J.A., Mendonça, M.T., Holt, D.E., & Johnston, C.E. (2015). Stress and auditory responses of the otophysan fish, *Cyprinella venusta*, to road traffic noise. *PLoS One*, *10*(9), e0137290. https://doi.org/10.1371/journal.pone.0137290
2. Fan, L., Zhang, L., Chen, D., Liu, G., & Wang, C. (2017). Research method about flow-induced noise in the bow of underwater vehicles (in Chinese). *Ship Science and Technology*, *39*(13), 48–53.
3. Herbert-Read, J.E., Kremer, L., Bruintjes, R., Radford, A.N., & Ioannou, C.C. (2017). Anthropogenic noise pollution from pile-driving disrupts the structure and dynamics of fish shoals. *Proceedings of the Royal Society B: Biological Sciences*, *284*(1863), Article 20171627. https://doi.org/10.1098/rspb.2017.1627
4. Huang, H., Yang, Y., Ruan, H., & Weng, J. (2023). Study about the correlation of very low frequency ocean noise with wind (in Chinese). *Journal of Applied Oceanography*, *42*(2), 255–263. https://doi.org/10.3969/J.ISSN.2095-4972.2023.02.009
5. Jia, F., He, R., & Xiang, Y. (2024). Experimental study of underwater noise HSD noise mitigation device for offshore wind turbine piles (in Chinese). *Marine Environmental Science*, *43*(3), 407–416.
6. Jiang, H., Wang, Y., Zhang, M., Hu, Y., Lan, D., Zhang, Y., & Wei, B. (2009). Locally resonant phononic woodpile: A wide band anomalous underwater acoustic absorbing material. *Applied Physics Letters*, *95*(10), Article 104101. https://doi.org/10.1063/1.3216805
7. Li, H., Cao, X., Shi, G., Zhang, X., Song, G., & Zhang, X. (2024). Research on sound insulation of floor support layer of high-speed trains based on phonon crystal (in Chinese). *Noise and Vibration Control*, *44*(1), 220–225.

8. Li, H., Guo, X., Song, G., Jia, Y., & Ma, L. (2022). Estimating the sound speed of the surface layer of the seabed using ocean ambient noise in shallow water (in Chinese). *Acta Acustica*, *47*(3), 348–355.

9. Lin, T., Liu, X., Wang, C., & Zhang, D. (2020). Effects of ship noise pressure level on swimming, feeding behaviors and immuno-physiological indicators of *Larimichthys crocea* juveniles (in Chinese). *Marine Fisheries*, *42*(1), 61–72.

10. Liu, H., Zhao, J., Yao, H., Han, D., Zhang, X., Wang, C., & Zhang, G. (2023). Bandgaps of a Helmholtz-type phononic crystal with adjustable chamber (in Chinese). *Journal of Synthetic Crystals*, *52*(4), 590–597.

11. Lu, Z., Zhu, X., Du, X., & Li, J. (2024). Development and prospect of deep-sea environmental noise monitoring technology (in Chinese). *Earth Science*, *49*(6), 2120–2130. http://doi.org/10.3799/dqkx.2023.162

12. Shi, H., Jiao, H., You, Z., Wang, Y., Li, S., Xu, J., & Yang, J. (2010). The effect of ship noise on the secretion of cortisol in *Lateolabrax japonicus* and *Pseudosciaena crocea* (in Chinese). *Acta Ecologica Sinica*, *30*(14), 3760–3765.

13. Wang, J., Zhou, H., & Zhang, J. (2022). Optimization design of low frequency sound absorption performance of local resonant cavity coating (in Chinese). *Ship Science and Technology*, *44*(22), 43–49.

14. Wu, J., Bai, X., Xiao, Y., Geng, M., Yu, D., & Wen, J. (2016a). Low frequency band gaps and vibration reduction properties of a multi-frequency locally resonant phononic plate (in Chinese). *Acta Physica Sinica*, *65*(6), Article 064602. http://doi.org/10.7498/aps.65.064602

15. Wu, J., Ma, F., Zhang, S., & Shen, L. (2016b). Application of acoustic metamaterials in low-frequency vibration and noise reduction (in Chinese). *Journal of Mechanical Engineering*, *52*(13), 68–78.

16. Yao, L., Xu, J., Jiang, G., & Wu, F. (2021). Band structure calculation of 2D fluid/solid and solid/fluid phononic crystal using a modified smoothed finite element method with fluid–solid interaction. *Ultrasonics*, *110*, Article 106267. https://doi.org/10.1016/j.ultras.2020.106267

17. Helal, K.M., Fragasso, J., & Moro, L. (2024). Effectiveness of ocean gliders in monitoring ocean acoustics and anthropogenic noise from ships: A systematic review. *Ocean Engineering*, *295*, Article 116993. https://doi.org/10.1016/j.oceaneng.2024.116993

18. Ye, L., Liu, Y., Liu, Y., Guo, J., & Yin, L. (2023). Study on behavior and physiology of low frequency vibration for *Larimichthys crocea* (in Chinese). *Fishery Modernization*, **50**(6), 1–8. https://doi.org/10.3969/j.issn.1007-9580.2023.06.001

19. Yin, J., Cai, L., Fang, X., Xiao, Y., Yang, H., Zhang, H., Zhong, J., Zhao, H., Yu, D., & Wen, J. (2022). Review on research progress of mechanical metamaterials and their applications in vibration and noise control (in Chinese). *Advances in Mechanics*, *52*(3), 508–586. http://doi.org/10.6052/1000-0992-22-005

20. Zhan, H., Li, X., Ni, M., Zhang, Z., Da, W., Wang, Y., Liu, Z., Liu, Y., He, C., Shi, X., & Liu, G. (2023). Research status and prospect of noise effect on fish (in Chinese). *Journal of Hydroecology*, *44*(6), 142–147.

21. Zhang, G., Gu, X., Xing, B., & Han, J. (2012). The classification and the impact of marine environment noise on marine animals (in Chinese). *Journal of Dalian Ocean University*, *27*(1), 89–94. https://doi.org/10.3969/j.issn.1000-9957.2012.01.018

22. Zhang, W., Yang, H., Ding, J., & Ji, X. (2017). The applicability research of offshore wind farm underwater noise propagation model (in Chinese). *Marine Sciences*, *41*(7), 78–86.

Manuscript received July 29, 2024; accepted for publication February 6, 2025; published online April 10, 2025.